



Distribution of magma beneath the Toba caldera complex, north Sumatra, Indonesia, constrained by three-dimensional *P* wave velocities, seismicity, and gravity data

Masturyono

Department of Earth and Environmental Sciences, Rensselaer Polytechnic Institute, Troy, New York
(mastur@bmg.go.id)

Meteorological and Geophysical Agency, Jakarta, Indonesia

R. McCaffrey, D. A. Wark, and S. W. Roecker

Department of Earth and Environmental Sciences, Rensselaer Polytechnic Institute, Troy, New York
(mccafr@rpi.edu; warkd@rpi.edu; roecks@rpi.edu)

Fauzi and G. Ibrahim

Meteorological and Geophysical Agency, Jakarta, Indonesia (fauzi@bmg.go.id)

Sukhyar

Volcanological Survey of Indonesia, Bandung, Indonesia

[1] **Abstract:** We estimate the one- and three-dimensional *P* wave velocity structure beneath the Toba caldera complex, a 30×100 km topographic depression in North Sumatra, using arrival time data of local earthquakes recorded by a 40-station seismic network that operated for 4 months. Inversions reveal the presence of *P* velocities up to 37% below normal that likely map the distribution of magma within this subduction-related volcanic system, considered the world's largest. In the upper 10 km of crust the largest low-velocity region underlies the southern two thirds of the depression and coincides with a gravity low centered over the resurgent dome. A smaller volume of low velocities is observed in the upper crust under the north end of the depression. Separating the two regions is a zone of locally high velocities, indicating that the shallow, subcaldera magma system is composed of two separate reservoirs, not a single one that extends the entire length of the caldera complex. Above each low-velocity region is a postcollapse volcano that erupted mostly mafic lavas after the last major caldera collapse ~ 74 kyr ago. A low-velocity column below one of these volcanoes can be traced into the uppermost mantle and corresponds with a planar distribution of low-frequency earthquakes in the 20- to 40-km-depth range. The low-frequency earthquakes apparently record the migration of melt in the mafic roots of this large-volume, crustal magma system.

Keywords: Magma; Sumatra; tomography; caldera; earthquakes; subduction.

Index terms: Lithosphere and upper mantle; volcano seismology; physics and chemistry of magma bodies; Asia.

Received July 12, 2000; **Revised** January 30, 2001; **Accepted** February 2, 2001;

Published April 16, 2001.

Masturyono, R. McCaffrey, D. A. Wark, S. W. Roecker, Fauzi and G. Ibrahim, and Sukhyar, 2001. Distribution of magma beneath the Toba caldera complex, north Sumatra, Indonesia, constrained by three-dimensional *P* wave velocities, seismicity, and gravity data, *Geochem. Geophys. Geosyst.*, vol. 2, Paper number 2000GC000096 [15,429 words, 8 figures, 3 tables, 3 appendix figures]. Published April 16, 2001.

1. Introduction

[2] The Toba caldera complex is located in North Sumatra, Indonesia, along the backbone of the Sunda arc (Figure 1). Situated within an oval-shaped, topographic depression that is 100 km long and 30 km wide, Toba is among the largest Quaternary caldera complexes known [Smith and Bailey, 1968]. The long axis of the depression is parallel to the arc and to the Sumatra Fault (SF), a right-lateral strike-slip fault extending from the Sunda Strait in the SE to the Andaman Sea off the NW end of Sumatra [Sieh and Natawidjaja, 2000]. The present outline of the depression formed 74,000 years ago during an eruption that spewed more than 2800 km³ of silicic pyroclastics over an area of at least 4,000,000 km² [Ninkovich *et al.*, 1978; Chesner and Rose, 1991]. Toba Lake, at an elevation of ~900 m above sea level, and up to 530 m deep [Knight *et al.*, 1986; Chesner and Rose, 1991], fills more than half of the depression. The resurgent dome is split into Samosir Island and the Uluan Block by a graben fault parallel to the long axis of the depression. Samosir Island, the western block, is ~45 km long and 20 km wide, and Uluan, the south-eastern block, is 35 by 15 km [Chesner and Rose, 1991].

[3] The position of Toba, along the Sunda arc and above a subducting slab, is consistent with the prediction that magma still occupies the crust below the caldera complex. The presence of magma is supported by the existence of hot springs along the western fracture, by post-74 ka resurgence of the depression floor, and by

local doming of the western margin of Samosir Island (Figure 1). The existence of the young (<74 ka) volcanoes Sipiso-piso and Pusubukit [Chesner and Rose, 1991] supports the inference that magmatism continues beneath Toba. Further support comes from large negative Bouguer gravity anomalies over Samosir Island [Nishimura *et al.*, 1984] that indicate low densities. In addition, Fauzi [1999] showed high attenuation of shear waves passing below Toba.

[4] In this study we develop one- and three-dimensional *P* wave velocity models for the crust and upper mantle below Toba by applying tomographic methods using local seismic data recorded by a temporary seismic network. Low velocities are used to infer the distribution of magma within the subcaldera system.

2. Eruption History

[5] Van Bemmelen [1939] and Aldiss and Ghazali [1984] suggested that the Toba depression formed during a single, large eruption, while Verstappen [1961], Yokoyama and Hehanusa [1981], and Nishimura *et al.* [1984] preferred a history of multiple eruptions and episodes of caldera collapse. This latter view is supported by the studies of Knight *et al.* [1986], Chesner *et al.* [1991], and Chesner and Rose [1991], who concluded that the Toba depression is a complex of overlapping calderas that collapsed during at least three major eruptions over a period of ~1 Myr. At ~0.84 Ma the Oldest Toba Tuff (OTT) erupted from a caldera centered near the south end of Lake

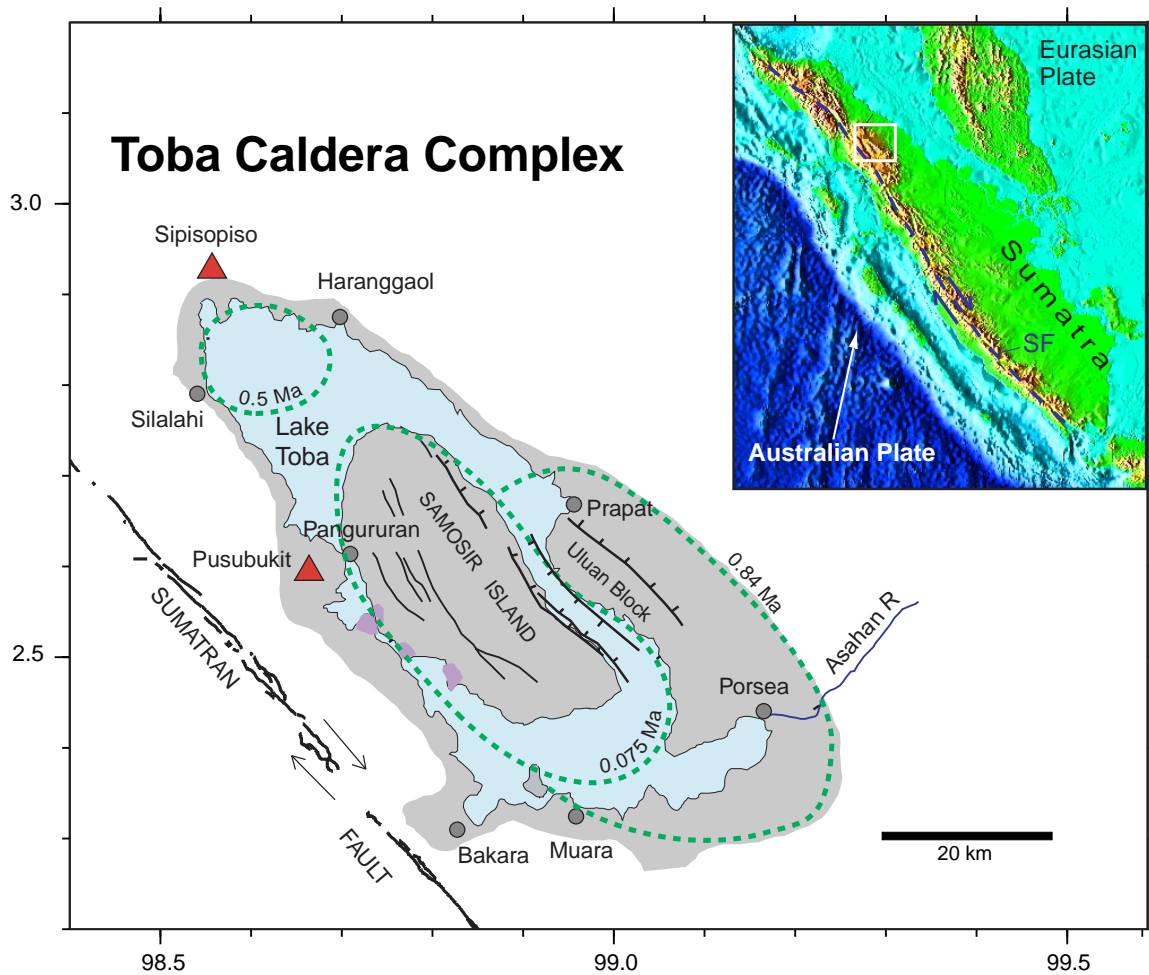


Figure 1. Toba caldera complex, North Sumatra, Indonesia, modified after *Knight et al.* [1986], with the gray region representing land within the present-day topographic depression. Dashed green lines show approximate source-caldera outlines for each of the three Toba tuffs, based on distribution of ash flow deposits, on work of *Knight et al.* [1986], and on reinterpretation of stratigraphy by *Chesner and Rose* [1991]. Red triangles show young dacite-andesite volcanoes. Areas of recent uplift are indicated by purple shading. The white box in the inset outlines the study area, and the arrow shows the direction of convergence of the Australian plate relative to the Eurasia plate [*DeMets et al.*, 1994].

Toba (Figure 1). The second eruption, at ~ 0.5 Ma, produced the Middle Toba Tuff (MTT) from a caldera at the northern end of the present-day depression. Finally, the huge eruption responsible for deposition of the Youngest Toba Tuff (YTT) took place at ~ 74 ka. Although thick, intracaldera deposits of YTT on Samosir Island indicate that the main

source was a caldera centered on the island; *Chesner and Rose* [1991] suggested that the YTT was erupted along the entire length of the depression from a laterally continuous magma body. The same authors also modified the interpretation of *Knight et al.* [1986] by including the 1.2-Ma Haranggaol Dacite Tuff (HDT), which originated at the northern end

of the lake, as a product of eruption from Toba.

[6] Volcanism and related activity continued after eruption of the YTT with formation of two largely andesitic volcanoes, Pusubukit and Sipiso-piso, on the western and northern shores, respectively, of Lake Toba. Post-YTT volcanism also included the formation of dacite lava domes (including Pardepur Island) at the southwestern end of the lake. In addition to regional uplift of the resurgent dome, small areas with sulfataric activity are actively being uplifted along the western margin of Samosir Island (Figure 1).

3. Arrival Time Data

[7] We operated a temporary seismic network around Toba (Figure 2) in cooperation with the Incorporated Research Institutions for Seismology (IRIS) Program for the Array Seismic Studies of the Continental Lithosphere (PASS-CAL) program and Indonesian scientific agencies. Details of the field program are given by Masturyono [2000] and are summarized here. The network was deployed for ~ 4 months, from late January to late May 1995. It comprised 30 short period (SP) and 10 broadband (BB) instruments, covering an area of about 250×250 km. The broadband stations were equipped with three-component Guralp CMG-3ESP seismometers and OMEGA clocks for time keeping. The short-period sites were equipped with three-component seismometers (Mark Product L22C-3D) and GPS for timing. Both the broadband and the short-period stations recorded continuously at 40 samples per second. The network recorded ~ 1500 local earthquakes from the subducting slab beneath Toba, from the Sumatra Fault, and from faults within the Toba depression, plus 130 regional earthquakes and 140 teleseisms.

[8] Broadband stations were located along the northeast side of the Toba depression parallel to

its long axis, on Samosir Island, and southwest of the depression (Figure 2). The BB seismograms are being used for a receiver function study [Armitage *et al.*, 1999]. A group of SP stations was placed southeast of Toba to record seismicity along the Sumatran fault zone. To obtain better control on the locations of intermediate-depth subduction zone events, one SP was installed in Nias Island, the largest island of the forearc ridge west of North Sumatra.

[9] *P* wave arrival times were picked from the vertical components of the digital data using Xphase, an interactive phase-picking tool (S. W. Roecker, Xphase manual, available at <http://gretchen.geo.rpi.edu/roecker/manuals/Xphase/Xphase.html>, 2000). Uncertainties of *P* wave picks are generally <0.1 s. Because the *S* to *P* converted phase can be mistaken for an *S* wave, *S* arrival times were picked from horizontal components only. The uncertainties of *S* arrival times are greater than those of *P* arrival times, but in most cases they are less than ~ 0.2 s. We also used arrival times from the eight-station, permanent, regional network operated by the Indonesian Meteorological and Geophysical Agency (MGA). Because those arrival times were picked manually from vertical-component paper records using a ruler, the uncertainties are estimated at 0.2 and 0.5 s for *P* and *S* arrival times, respectively. The MGA stations comprise a small fraction of the data used.

[10] To cull unreliable arrival times, we determined preliminary locations of the local earthquakes using the one-dimensional (1-D) *P* velocity model used by Fauzi *et al.* [1996] and an *S* velocity model derived from modified Wadati plots using shallow and intermediate depth events. *P* arrival times with residuals of more than 2.0 s were removed from the data set. The earthquakes included in the inversion passed the following criteria: at least 6 *P* waves and at least 2 *S* arrivals, and the rms of the travel time residuals of the preliminary location

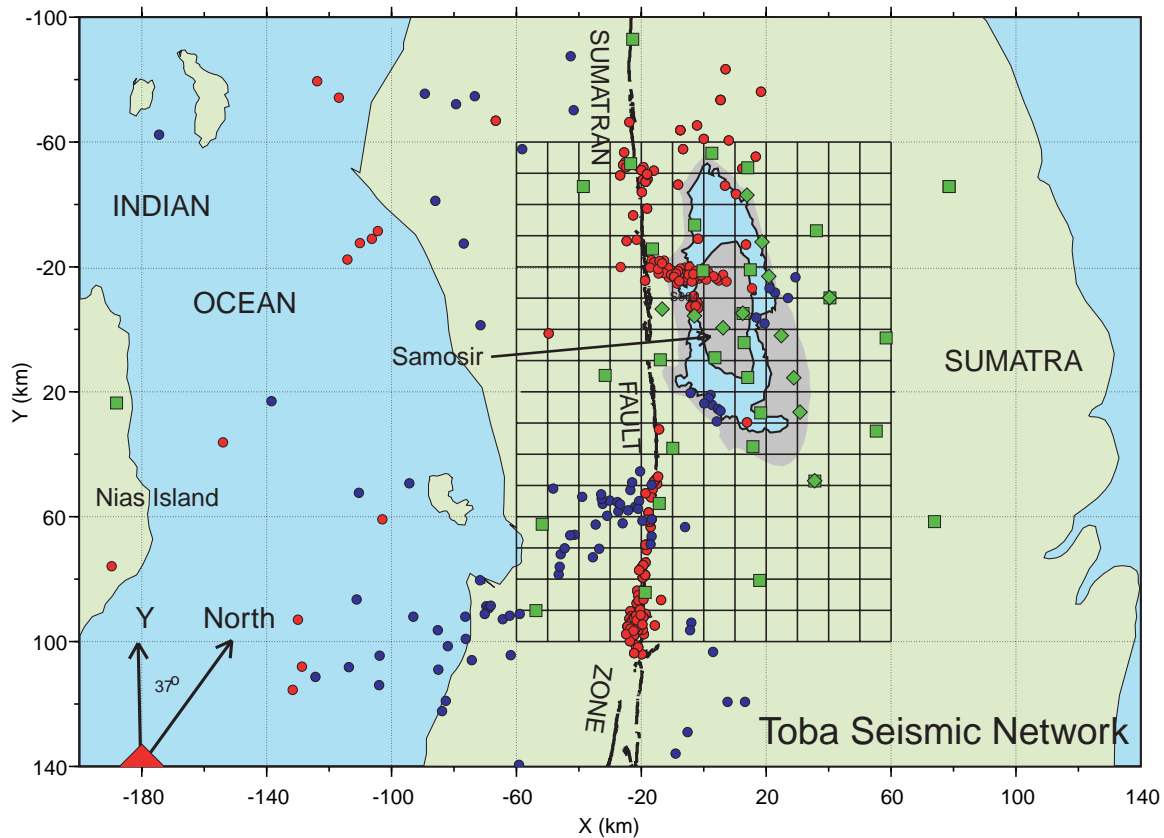


Figure 2. Distribution of seismograph stations (diamond, broadband; square, short period) and local earthquakes (blue and red dots) used for tomographic inversion (red dots represent quakes in the 0–45 km depth range, and blue dots are for the 45–200 km range). The mesh shows the outline of the velocity model region. The center of the mesh is at 2.5°N, 98.8°E. The orange region shows the present-day topographic depression at Toba, and dark blue is the region covered by the lake.

is <1.5 s. This selection process left about 4000 P and 2700 S arrivals for the inversion.

4. Inversion Method

[11] We used the inversion code SPHYT90 of S. W. Roecker (Sphypit90 manual, available at <http://gretchen.geo.rpi.edu/roecker/manuals/sphypit90/Sphypit90.html>, 1997), a modification of the *Aki and Lee* [1976] scheme, to develop both one- and three-dimensional velocity models. This implementation of the seismic tomography method has been used many times to determine velocity structures else-

where, and detailed explanations can be found in those papers [Roecker *et al.*, 1987; Shedlock and Roecker, 1987; Abers and Roecker, 1991; Roecker *et al.*, 1993; Jones *et al.*, 1994]. In general, seismic tomography has been used extensively to study velocity structures beneath other volcanic regions [Steck *et al.*, 1998; Lutter *et al.*, 1995; Roberts *et al.*, 1991; Ankeny *et al.*, 1986; Weiland *et al.*, 1995; Steck and Prothero, 1994; Dawson *et al.*, 1990]. Here the method used in this study is discussed briefly.

[12] The residual (r_{ij}), the difference between the expected and observed arrival time of local



earthquake i to station j , can be described in the linear hypocenter-velocity problem as

$$r_{ij} = \sum_{i=1,4} \delta t / \delta h_i \Delta h_i + \sum_{j=1,M} \delta t / \delta s_i \Delta s_j, \quad (1)$$

where $\delta t / \delta h_i$ is the partial derivative of arrival time with respect to the four hypocenter parameters (latitude, longitude, depth, and origin time) and $\delta t / \delta s_i$ is the partial derivative of the arrival time with respect to wave slowness. In matrix form, (1) is written as

$$r = \mathbf{A} \Delta h + \mathbf{B} \Delta s, \quad (2)$$

where matrices \mathbf{A} and \mathbf{B} contain hypocenter and velocity derivatives, respectively. To reduce the number of parameters, the hypocenter term in (2) is eliminated using parameter separation [Pavlis and Booker, 1980]. The forward problem is then written as

$$d = g(p_{\text{true}}), \quad (3)$$

where d contains the arrival times, p_{true} contains the true slownesses, and g is the functional relation between d and p . The slownesses are estimated iteratively using the following formula from Tarantola and Valette [1982]:

$$p_{k+1} = p_k + (\mathbf{G}_k^T \mathbf{C}_{dd}^{-1} \mathbf{G}_k + \mathbf{C}_{pp}^{-1})^{-1} \times \{\mathbf{G}_k^T \mathbf{C}_{dd}^{-1} [d - g(p_k)] - \mathbf{C}_{pp}^{-1} (p_k - p_0)\}, \quad (4)$$

where p_0 contains the initial estimate of slownesses, p_k is the estimate of the slownesses at the k th iteration, \mathbf{G}_k is the a matrix of partial derivatives (dg/dp_k), \mathbf{C}_{dd} is the data covariance matrix, and \mathbf{C}_{pp} is the model covariance matrix. The origin times and hypocenters are determined in a separate step prior to the inversion for the velocities. Ray paths and travel times are estimated with an approximate ray-tracing technique [Thurber and Ellsworth, 1988].

5. One-Dimensional Velocity Model

[13] To delineate the distribution of velocity anomalies beneath Toba, we first use the arrival time data to estimate a one-dimensional veloc-

ity structure beneath the Toba region. To facilitate comparison of the estimated velocities to “normal” crustal structure, we define a reference structure (Table 1) using a combination of nearby refraction profiles and typical continental crust (Figure 3a). Marine seismic refraction profiles west of north Sumatra [Kiekhefer, 1980] provide estimates of normal P velocities in the crust and upper mantle beneath Sumatra. In a shallow-water, near-shore reversed profile on the Sunda Shelf (INDO1310/11), the upper 8.3 km of crust showed an average P velocity of 5.6 km/s. A layer with $V_p = 6.8$ km/s was found at 10 km depth, and the Moho was not reached in that profile. Farther offshore, the unreversed refraction profile in the 600-m-deep Nias Basin (profile INDO1308/09) showed a layer of $V_p = 6.5$ km/s at 19.6-km depth and the Moho at 22.9-km depth, assuming a velocity of 8.1 km/s. We estimate the nominal depth of the Moho beneath the island of Sumatra by assuming isostatic equilibrium and densities of 2700 kg/m³ for the crust and 3300 kg/m³ for the upper mantle. If the Moho is 22 km deep beneath the Nias Basin where the water depth is 0.6 km, then its equilibrium depth should be ~ 29 km beneath the Sumatra mountain range where the elevation is ~ 1 km above sea level.

[14] Our reference model, also used as a starting model, based loosely on the refraction results and on IASPEI91 [Kennett, 1991], comprises three crustal layers that have an average velocity that is 3% faster than the upper 40 km of the

Table 1. Regional One-Dimensional Reference Velocity Model

Layer Depth Extent, km	V_p , km/s	V_s , Km/s
–2 to 10	5.3	3.1
10 to 24	6.5	3.8
24 to 40	7.4	4.3
40 to 65	8.1	4.7
65 to ∞	8.1	4.7

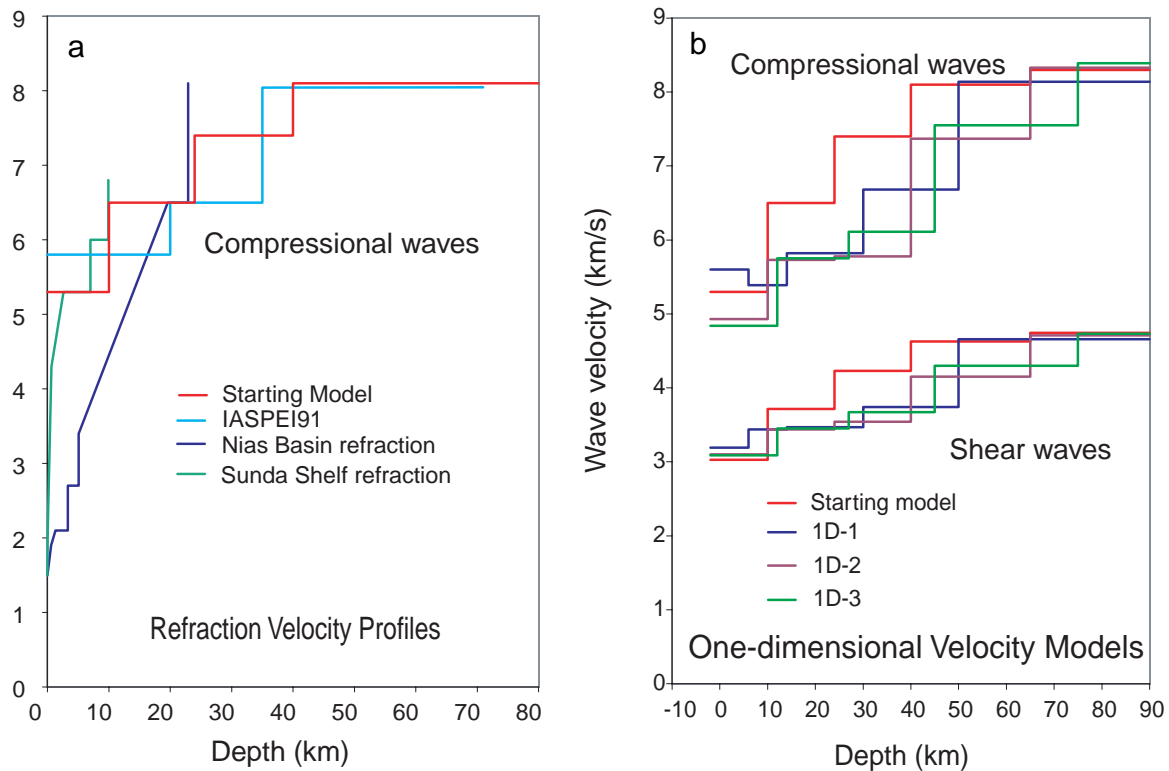
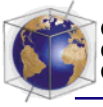


Figure 3. (a) Summary of velocity-depth profiles used to infer a regional reference velocity model. The refraction lines are from *Kieckhefer* [1980], and IASPEI91 is a globally derived model [Kennett, 1991]. The red line shows our reference model. (b) Results of inversions for one-dimensional velocity profiles compared to reference model. The three inversions start with different layer thicknesses, and all show low velocities relative to the reference model.

IASPEI91 model (Figure 3a). The model has $V_p = 5.3$ km/s above 10-km depth, $V_p = 6.5$ km/s from 10- to 24-km depth, and $V_p = 7.4$ km/s from 24-km depth to the assumed Moho at 40 km. We overestimate the Moho depth in the starting model so that we do not later interpret normal lower crustal velocities as anomalously low mantle velocities. Furthermore, our series of one-dimensional inversions using varied layering suggest that the largest velocity jump that could be attributed to the Moho is closer to 40 km than to 30 km. We assume that the thermally unperturbed mantle velocity is 8.1 km/s. The shear wave reference model is derived from the P wave model with a Poisson's ratio of 0.25 ($V_p \approx 1.73 V_s$).

[15] To estimate the variation of seismic velocities with depth, the structure below the study area is represented by horizontal layers of uniform velocity. Consequently, in representing a true velocity structure that varies smoothly with depth, the velocity assigned to any given layer will be some approximate average of the velocities over the depth range of the layer. We used a five-layer model: the starting model comprises three layers with crustal velocities and a layer of uppermost mantle velocity overlying a mantle half-space. The top layer was extended to 2 km above sea level to include all the seismograph stations and precluding the necessity of station elevation corrections. Several combinations of the thicknesses and the

depths of the interfaces were tested [Masturyono, 2000]. The inversion for P and S velocities of the layers was run iteratively until the variance was reduced by <1% or increased relative to the previous iteration.

[16] Model misfits are quantified by the ratio of the final weighted misfit variance to the a priori data variance (0.051 s^2), a measure of the expected noise in the data based on the assigned weights [Bevington, 1969, p. 73]. This ratio, which we call χ_n^2 , is equivalent to $N^{-1} \sum_i = 1, N w_i r_i^2$, where N is the number of observations, w is the weight of the observation ($w = \sigma^{-2}$), and r is the residual. The overall final χ_n^2 for the arrival time misfits for the tested 1-D models ranged from 1.94 to 3.00. That these are considerably larger than 1 indicates that the data are not overfit by the 1-D models and that 3-D modeling is warranted. Model 1D-2 (Figure 3b) gives the best fit to the data, and the final variance is about half of that for the starting model (χ_n^2 for the starting model is 3.79). The formal uncertainties in the 1-D velocities are all very small (<0.03 km/s), reflecting an abundance of data, but they do not take into account our ignorance of the layer thicknesses. In other words, the travel-time data could resolve very well the velocity of a layer of constant velocity and known thickness.

[17] All 1-D solutions show large decreases in velocities relative to the starting model (Figure 3b). The largest jump in the velocities, which may signal the Moho, appears to occur between the third and fourth layers, whose boundary ranges from 40 to 50 km depth in the trial models. Some 1-D solutions show the presence of a low-velocity layer in either the middle or the lower crust. Because the P velocities beneath the entire study area are low, we compare model velocities to our estimate of unperturbed velocity structure outside the study area (the reference model) instead of to the averages determined by tomography within the

study area. By doing this, we expect to get a better estimate of the total thermal perturbation to the velocities that are subsequently interpreted in terms of magmatic source volumes. However, it should be kept in mind that our estimates of normal unperturbed velocities are only approximate and the percent changes we quote may be off by several percent.

[18] Compared to the reference P velocities of the crust and the upper mantle, the final average P velocities of layers within the study area are lower by about 2–16%, 9–22%, and 6–15% for models 1D-1, 1D-2, and 1D-3, respectively (Figure 3b). The shear wave velocities show a similar trend; they are up to 20%, 17%, and 14% lower for the three models with the lowest values falling in the lower crust (Figure 3b). That the S fractional anomalies are similar to the P indicates that Poisson's ratio is not severely altered. This indicates that each layer is, on average, dominated by solid phases but still allows the possibility of largely liquid (melt) domains on a smaller scale. We selected the three 1-D models shown in Figure 3b to use as initial models to generate the 3-D model. In addition to the best fit model 1D-2, models 1D-1 and 1D-3 were selected because their layering differs from model 1D-2.

6. Three-Dimensional Velocity Model

6.1. Approach

[19] To address the questions involving the lateral distributions of magma, we derive three-dimensional velocity models from the same data set used above. We divided the study volume into rectangular prisms. Because most surface geological features near Toba are oriented NW-SE, one axis of the model coordinate system is oriented N37°W and the other is oriented N53°E (Figure 2). Taking the distribution of the stations and ray paths into consideration, we chose 10 km for the horizontal

Table 2. Normalized Variances and Average Diagonal Matrix of Shifted Models

Model	χ_n^2	Average Resolution
3D-2	1.22	0.74035±0.00023
3D-2X2.5	1.38	0.63483±0.00023
3D-2X5	1.29	0.63185±0.00023
3D-2X7.5	1.30	0.61119±0.00023
3D-2Y2.5	1.30	0.65287±0.00023
3D-2Y5	1.33	0.64784±0.00023
3D-2Y7.5	1.29	0.65185±0.00023

dimension of the blocks, and the layer thicknesses followed the one-dimensional initial models. Each layer is divided evenly into 9×14 blocks. We ran several trial inversions using different block sizes and evaluated the ray coverage.

[20] To test the dependency of the final three-dimensional model on the choice of the starting model, we started with each of the three one-dimensional models. We ran each inversion for five iterations or until the variance increased relative to the previous iteration. The final χ_n^2 are 1.29, 1.22, and 1.25 for models 3D-1, 3D-2, and 3D-3, derived from starting models 1D-1, 1D-2, and 1D-3, respectively. Similarity of the main velocity patterns in the final 3-D models suggests that they do not depend on the starting models [see Masturyono, 2000]. The differences between the average V_p for each layer in the 3-D models and the initial 1-D models are <1%, except for the upper crust, indicating consistency between the 3-D solutions and the initial 1-D models.

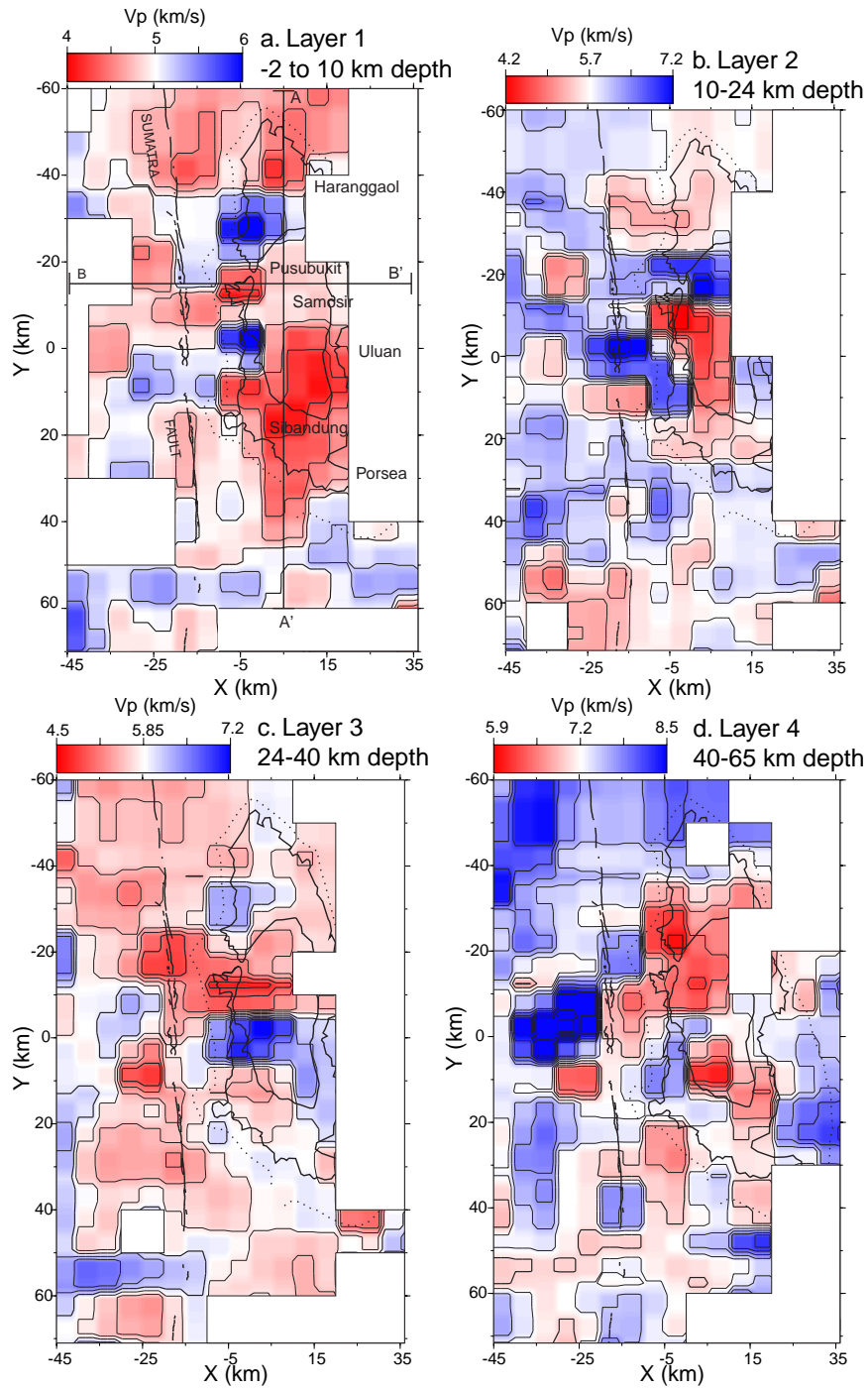
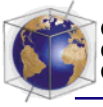
[21] For further analysis, we selected model 3D-2 both because its misfit variance in the last iteration is the smallest and because the initial model, 1D-2, does not include a low-velocity layer within the crust (Figure 3b). The latter consideration precludes that the low-velocity layer in the three-dimensional model is predetermined by the presence of low velocity in the initial model. The posi-

tions of the horizontal interfaces and the thicknesses of the crustal layers of 3D-2 are between those of 3D-1 and 3D-3. For these reasons, we use 3D-2 as representative of the three models.

[22] Because we use blocks to model the structure, the inversion result may be influenced by the placement of the block boundaries. Accordingly, we ran seven different configurations of 3D-2 while shifting the X axis or Y axis or both by 2.5 km. The variance ratios and average resolutions of such tests (Table 2) show that model 3D-2, without shifting, fits best. We then averaged models to reduce the bias due to choice of placement of the vertical interface boundaries. Solution 3D-2 (Figure 4) is combined with models 3D-2X5 and 3D-2Y5. (Models 3D-2X5 and 3D-2Y5 were formed by shifting the X and Y axes, respectively, of the block boundaries by 5 km, or one half the block size, from 3D-2.) Averaging reduces the effective dimension of lateral blocks from 10×10 km to 5×5 km. Although the purpose of the averaging is to reduce the bias in the placement of the interface boundaries, it also smoothes the model by reducing the velocity contrasts between adjacent blocks.

6.2. Results

[23] The average V_p in the upper 10 km of the crust (Figure 4a) is 4.90 km/s, 7% below the reference velocity for the upper crust in this region. Velocities are not uniform: two principal regions of anomalously low V_p are seen. A large area (about 15×40 km) of low V_p underlies the southern two thirds of Toba (including the entire island of Samosir) with the lowest velocities (4.2 km/s, or ~21% below normal) at the southern end of the island and below the southern part of the lake. Within this broad low a second local low V_p (4.1 km/s, ~23% below normal) is



found below the north end of Samosir in the vicinity of Pusubukit volcano, near the western edge of the island. A separate region of low V_p (~ 4.3 km/s, 19% below normal) underlies the northern end of Lake Toba, extending northward beyond the depression margins to include the crust below Sipisopiso volcano. The two low-velocity regions are separated by a relatively high V_p zone reaching 6.0 km/s (13% above normal) just north of Samosir.

[24] The regions of low V_p recognized in the upper crust extend into the middle crust (10–24 km depth), where the average V_p is 5.76 km/s, $\sim 11\%$ below normal (Figure 4b). The broadest low- V_p region is, however, more focused in the middle crust. Velocities are again as low as 4.1 km/s ($\sim 37\%$ below normal) but are concentrated in a single, N-S elongate zone that underlies southwestern Samosir (Figure 4b), which then bends westward toward the margin of the depression on the south side of Pusubukit. As in the upper crust, a high-velocity region separates this zone from the low- V_p region at the northern end of the depression.

[25] The average P velocity in the lower crust (24–40 km depth) is ~ 5.73 km/s, 23% below normal V_p for this region (Figure 4c). Lowest V_p values are again found beneath the western margin of Samosir and Pusubukit (4.7 km/s, 36% below normal), although the lateral dimensions of this region are smaller and are aligned in a WNW-ESE direction (Figure 4c). As recognized at shallower crustal levels, rela-

tively high V_p regions lie just to the north and south of this low-velocity zone.

[26] Finally, V_p values in what we consider to be the uppermost mantle (40–65 km depth) average 7.36 km/s, 9% below the V_p in normal upper mantle. A broad region of low V_p (to 6.0 km/s; 26% below normal) is centered in the vicinity of Pusubukit, with another, more focused area under southern Samosir (Figure 4d).

6.3. Velocity Structure in Areas of Low Resolution

[27] The resolution of P velocities along the east side of the depression is low (diagonals of the resolution matrix are <0.5), but other data suggest that the low velocities extend here as well. Fauzi [1999] studied the attenuation of seismic waves in North Sumatra using seismic data recorded by a permanent regional seismic network. One-dimensional models of seismic wave attenuation show low Q beneath two stations at the east and southeast edges of Toba. Fauzi [1999] suggested that the depth of magma beneath those stations is <20 km. Preliminary results of receiver function studies using broadband seismograms recorded by the Toba network show low S wave velocity beneath the stations all along the eastern rim of the depression [Armitage *et al.*, 1999]. This result is consistent with Fauzi's low Q values beneath the east side. The depth of the magma system beneath the middle of Samosir island extends to the lower crust, consistent with the low S wave velocity at 10–35 km depth

Figure 4. Three-dimensional P velocity model. Outline of the model is shown in Figure 2 (only the resolved part of the model domain is shown here). The final model is an average of models 3D-2, 3D-2X5, and 3D-2Y5 (see text for detailed explanation). The contour interval is 0.25 km/s, and selected contours are labeled. Blocked out regions (white) are those not resolved. Dashed line shows the outline of the Toba depression. (a) Velocities for layer 1, from the surface to 10 km depth. Lines AA' and BB' show cross sections of Figure 5. (b) Velocities for layer 2, from 10 to 24 km depth. (c) Velocities for layer 3, from 24 to 40 km depth. (d) Velocities for layer 4, from 40 to 65 km depth.

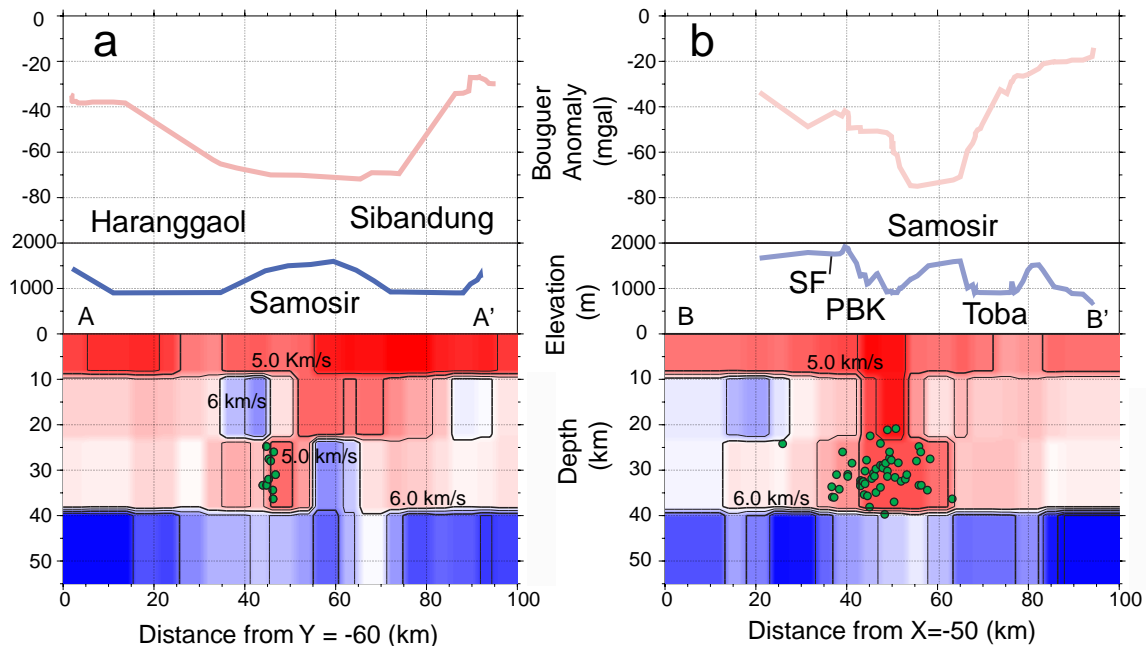
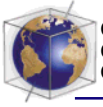


Figure 5. (a) NW-SE and (b) SW-NE trending cross sections showing gravity, topography, and tomography results. Profile locations are shown in Figures 4a and 7. Green dots show projections of long-period earthquakes onto the cross sections. PBK, Pusubukit; SF, Sumatra fault.

revealed by receiver function analysis [Armitage *et al.*, 1999].

6.4. Low-Frequency Earthquakes Beneath Toba

[28] Local earthquakes recorded by the Toba seismic network were relocated using the final three-dimensional velocity model 3D-2. Of particular interest, some earthquakes form a line perpendicular to the Sumatran fault, extending eastward below Pusubukit volcano and across the western margin of Toba, where they end beneath the resurgent dome (Figure 2). These earthquakes, at 20–40 km depth, coincide with low P velocities beneath Pusubukit (Figure 5). No similar events are found within the low-velocity regions to the north or south. Spectral analysis of the wave forms shows that the dominant frequencies of these events are ~ 2 –4 Hz (Figure 6c) and are independent of

the station-epicenter distance and azimuth (Figures 6a and 6b). Earthquakes outside this small region beneath Pusubukit show higher frequencies (Figures 6c, 6d and 6e). Hence we think that the low frequencies are a property of the source mechanisms and are not due merely to attenuation along the propagation path. While the low-frequency and emergent nature of the seismograms lead to larger uncertainties in the arrival time picks, we suggest that the small amount of scatter in the hypocenters in both map view (Figure 2) and cross section perpendicular to the trend (Figure 5a) indicates that the events are correctly located within a couple of kilometers.

[29] Low-frequency (LF) earthquakes in the 20–60 km depth range have been observed in volcanic regions elsewhere (Table 3). Beneath central and northeastern Japan, LF earthquakes occur within and near zones of low P velocities

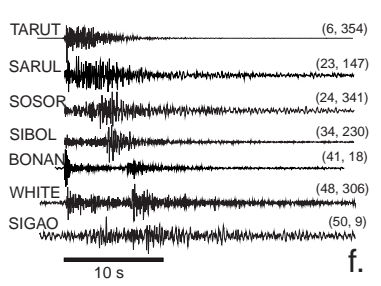
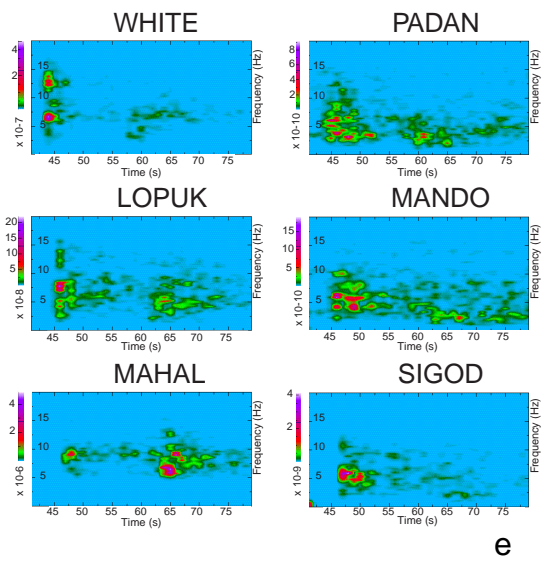
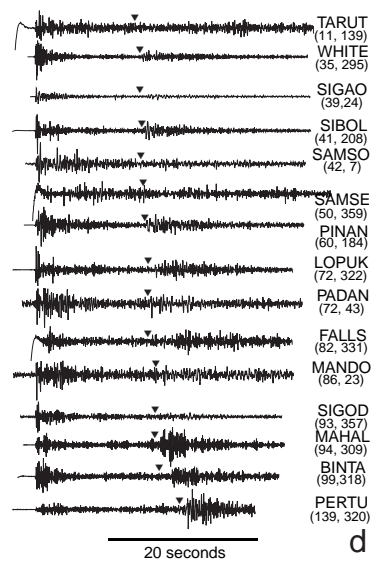
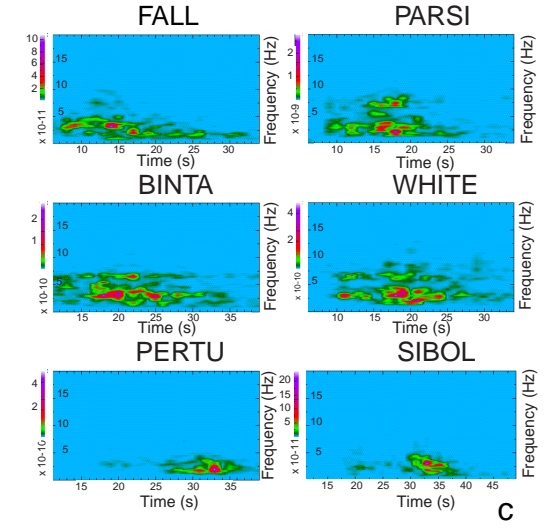
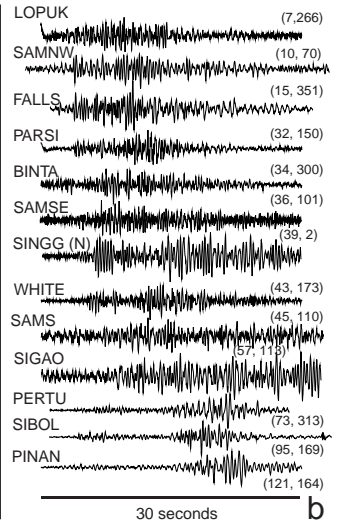
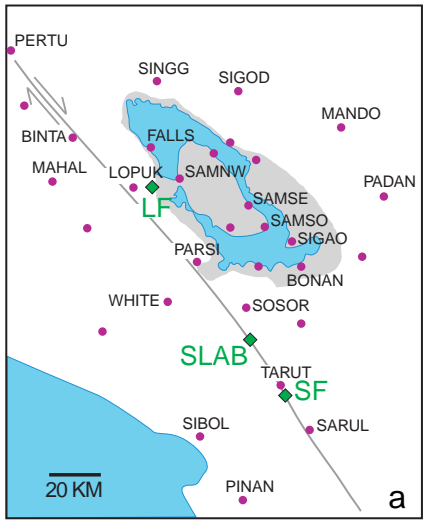


Table 3. Deep Crustal Long-Period Earthquakes Beneath Volcanic Regions

Volcano Location	Dominant Frequency, Hz	Depth, km	References
Mount Pinatubo, Philippines	2.0–3.9	28–35	<i>White and Dzurisin</i> [1997]
Kilauea, Hawaii	-	30–60	<i>Okubo</i> [1997],
	0.8–2.5	10	<i>Warren et al.</i> [1997]
Central Japan	1–5	25–45	<i>Ukawa</i> [1997]
Northeast Japan	1–5.5 (<i>P</i>)	25–40	<i>Hasegawa et al.</i> [1997]
	1.5–4.5 (<i>S</i>)		
Mammoth Mountain, California		10–20	<i>Pitt and Hill</i> [1997]
St. Helens and Mount Baker, Washington	2–3 Hz	20–30	<i>Malone</i> [1997]
Mount Spurr, Alaska	1–3 Hz	20–40	<i>Power et al.</i> [1997]

revealed by tomography [Ukawa, 1997; Hasegawa *et al.*, 1997]. LF earthquakes occurred prior to the eruptions of Mount Pinatubo in 1991 [White and Dzurisin, 1997] and Mount Spurr in 1992 [Power *et al.*, 1997]. Beneath Kilauea Volcano, such earthquakes are interpreted as a manifestation of magma transport [Aki and Koyanagi, 1981; Okubo, 1997].

[30] Although the low-frequency earthquakes beneath Toba were not followed by surface volcanic activity, their waveforms are similar to those of LF earthquakes associated with active magma systems elsewhere. This similarity, and the correlation of the Toba earthquakes with regions of low *P* velocities, is interpreted to indicate that they record migration of ascending, relatively mafic (and therefore mantle-derived) melt. This interpretation is consistent with the type of lavas erupted from Pusubukit, which formed by mixing of dacite from the same upper crustal, large-volume

reservoir that fed earlier YTT eruption, with andesite or basaltic andesite melts [Wark *et al.*, 2000].

6.5. Gravity Anomalies Around Toba

[31] Compiled Bouguer gravity anomalies (BA) are generally low near Toba, reaching approximately -75 mgal over Samosir island (Figures 5 and 7). The low-gravity field can be explained in a number of ways: (1) Airy-type isostatic compensation (crustal root) for the topographic elevation of the Batak Tumour, (2) a thick layer of tuff with lower density than normal crustal rocks, or (3) low-density crustal rocks due to thermal expansion.

[32] The expected Bouguer gravity anomaly due to a compensating crustal root is approximately $\Delta g = -2\pi G\rho_c h_c$, where G is the gravitational constant, ρ_c is the density of the crust, and h_c is the height of the topography.

Figure 6. Examples of vertical-component seismograms and spectrograms of earthquakes. (a) Map showing locations (green diamonds) and seismograph sites for low-frequency event (LF), slab event (SLAB) and Sumatra fault event (SF). Labeled sites have seismograms shown. (b) Seismograms of the low-frequency (LF) event at 37 km beneath the west side of Toba. Numbers in parentheses are the epicenter-station distance in kilometers and the azimuth from the epicenter to the station in degrees. (c) Spectrograms show the frequency content of the seismograms as a function of time. These events show most energy at frequencies lower than 5 Hz at all sites. (d) Seismograms for an earthquake at 132 km depth in the subducted slab south of Toba. Inverted triangles show the predicted arrival of the *S* waves. Note that shear waves at stations to the north are largely attenuated. (e) Spectrograms for a slab event show frequencies in the 5–10 Hz range. (f) Seismograms for a shallow event (8 km depth) on the Sumatra fault south of Toba.

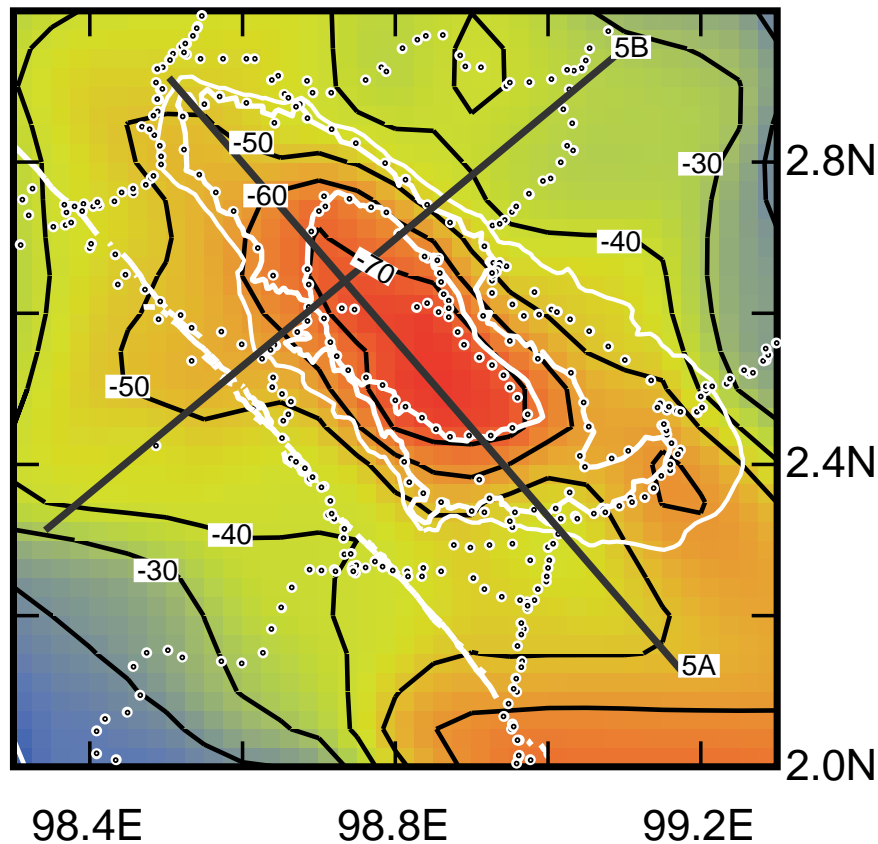


Figure 7. Bouguer anomaly map. The contour interval is 10 mGal, and the small dots show observation points. Lines show cross sections of Figure 5 as labeled. The white curves show outlines of the present-day topographic depression at Toba, of the lake, of Samosir Island, and of the Sumatra fault.

Assuming $\rho_c = 2600 \text{ kg/m}^3$, $\Delta g = -109 \text{ mGal}$ for an average of 1 km of topography; hence the topography around Toba is undercompensated.

[33] A second possible explanation of the low gravity is the low-density tuff layer on Samosir Island. In this case the gravity anomaly will be approximately (for an infinite sheet) $\Delta g = 2\pi G(\rho_c - \rho_t)h_t$, where ρ_t is the density of the tuff and h_t is the thickness of the tuff. Nishimura *et al.* [1984] estimated the density of Toba Tuff on Samosir Island to be 2100 kg/m^3 . Using $\rho_t = 2100 \text{ kg/m}^3$, the thickness of the tuff layer is at most 3.6 km. To take into account the finite extent of the tuff and a

more realistic distribution of it, we estimate the gravity anomaly for a “2.5-dimensional” model (i.e., the third dimension is finite but symmetric about the cross section). The tuff body is 60 km long parallel to the long axis of the depression and 20 km wide. A thin layer of tuff to the west (650 m thick) and east (250 m thick) of the depression (thicknesses based on stratigraphic sections of Chesner and Rose [1991]) with lower density than that of the tuff on Samosir are taken into account for the gravity calculation. In this case the observed gravity anomaly can be fit with $2.5 \pm 0.2 \text{ km}$ of low-density tuff on Samosir (Figure 8a).

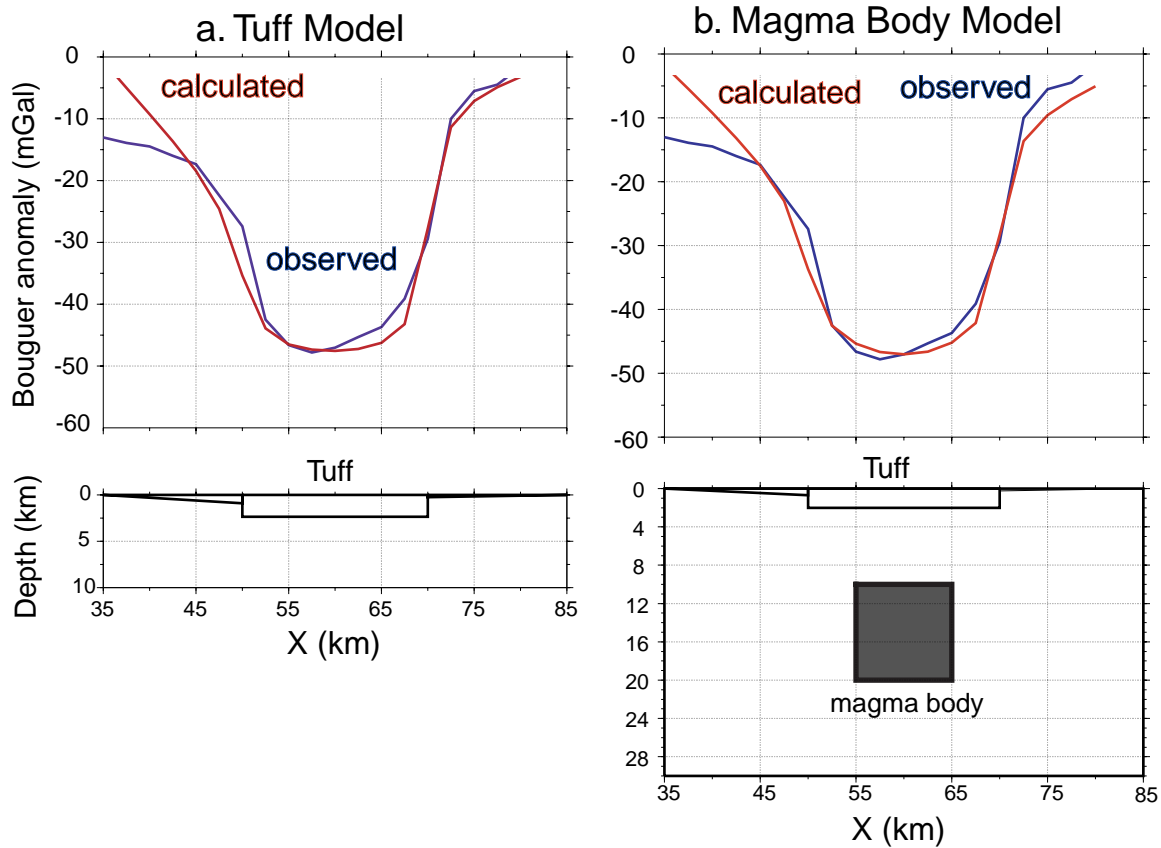


Figure 8. SW-NE gravity profiles and corresponding tuff and magma body models. (a) Model in which gravity anomaly over Samosir Island is matched by tuff only. The tuff is 2.5 km thick with a density contrast of 500 kg/m³. (b) An example of a two-dimensional crustal magma body that also explains the low gravity over the Samosir. The magma body is 10 × 10 km in cross-sectional area, centered at 15-km depth, with density contrast of 170 kg/m³; the thickness of tuff in this figure is 2.0 km with density contrast of 500 kg/m³. Tuff layer with density contrast of 650 kg/m³ is tapered to the SW and NE of the depression in both models to match regional gravity.

[34] Finally, noting that the low velocities beneath Toba are likely associated with high temperatures, the observed low gravity may in part be caused by the presence of a low-density magma body within the crust (Figure 8b), as suggested by the correlation of low gravity with low velocities in Figure 5. The gravity anomaly due to a magma body is approximately (again for an infinite sheet) $\Delta g = 2\pi G(\rho_c - \rho_m)h_m$, where ρ_m is the density of the magma body and h_m is its thickness. For constraints on magma density

we cite experiments done by *Murace and McBirney* [1973] that show density fluctuations of Mount Hood andesite caused by temperatures between 800°C and 1400°C to be ~190 kg/m³. Assuming $\rho_c - \rho_m = 190$ kg/m³, the thickness of a magma body required to cause a -75 mGal anomaly is ~9 km. For a lower-density contrast the magma body needs to be correspondingly thicker. The tomography results suggest that the low velocities and therefore low densities extend over 50 km or more in depth, in which case the

density perturbations due to warming need to be only 40 kg/m³ or so to explain the gravity anomalies.

[35] In summary, the gravity anomaly can be explained by either a crustal root, near-surface tuff or by warm, low-density crust at greater depth. The tomography results suggest that thermal expansion of the crust and upper mantle adds to the gravity anomaly, but we cannot independently demonstrate this from the gravity data alone.

7. Discussion

7.1. Upper Crustal Magma Distribution

[36] Our tomographic study provides the first three-dimensional image of *P* velocity structure beneath Toba. Reflecting its recent history of volcanic and hydrothermal activity, the region as a whole exhibits relatively low velocity compared with “normal crust.” In the upper 10 km of crust, however, particularly low velocities are present in two broad regions that are separated by a relatively high-velocity zone. The larger of the two regions encompasses much of the southern two thirds of the depression, including the resurgent dome, Samosir Island. Velocities are lowest near the southern end of Samosir and below Pusubukit volcano, one of the two young volcanoes that formed near the margin of the Toba depression after YTT eruption 74 kyr ago. The smaller of the two low-velocity regions, which includes the post-YTT volcano Sipiso-piso, underlies the northernmost end of the Toba depression.

[37] Each of the two low-velocity regions is reasonably interpreted to contain magma or residual heat from a preexisting magma body. That the low velocities are related to presence of magma, at least in part, is consistent with the young age of the caldera complex,

its location in an active volcanic arc, and the recent uplift and hydrothermal activity on parts of the resurgent dome. Indirect evidence of molten rock is provided, too, by strong attenuation of shear waves [Fauzi, 1999; this study, Figure 6d]. With this in mind, we interpret the broad, southern low-velocity region, and probably the smaller region of low velocity to the north, to outline the main, silicic magma bodies that fed earlier caldera-forming eruptions of silicic ash flow tuff.

[38] The presence of a relatively high velocity region separating the northern and southern low-velocity zones, which persists to deeper crustal levels, appears to indicate two separate upper crustal magma systems. This contrasts with the suggestion of Chesner and Rose [1991] that Toba was underlain by, and YTT was erupted from, a single, large magma body that extended the length of the depression. The presence of two separate systems is consistent, however, with the work of Knight *et al.* [1986], who concluded that throughout the 1-Myr history of eruptions from Toba, there was never a single caldera on such a large scale. Instead, their work suggests that all major eruptions originated from smaller structures situated either to the north or to the south of a line roughly corresponding with the trace of the high-velocity region (Figure 4). Indeed, the outlines of the smaller calderas proposed by Knight *et al.* [1986] roughly correspond with the low-velocity regions that we identify in the upper crust.

[39] The low velocities that characterize the upper crust below the two post-YTT volcanoes may also be attributed to residual silicic magma or to relatively mafic melts like those that make up the bulk of erupted material at each. We favor the former interpretation on the basis of the fact that at each volcano,

dacite lavas are among erupted products [Wark *et al.*, 2000].

7.2. Roots to the Crustal Magma System

[40] At midcrustal levels (10–24 km depth) the regions of low velocity that characterize the upper crust can still be recognized. The midcrust velocity anomalies at the northern end of the Toba depression are not as strong as they are at shallower levels, however. Similarly, the broad upper crustal region of low velocity below the southern end, which is believed to outline the main silicic magma reservoir, is smaller in extent and is shifted northwestward in the middle crust, where it appears continuous with the strong, highly focused region below Pusubukit, where the lowest midcrustal velocities are found. In the lower crust (Figure 4c) the lowest velocities are still below Pusubukit, where they occupy a narrow, elongate zone trending WSW-ENE that corresponds with the plane of low-frequency earthquakes (Figure 5). Low velocities also characterize the uppermost mantle below this zone.

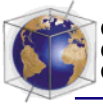
[41] We interpret the low-velocity “column” below Pusubukit to trace the main path of ascending, mantle-derived melts that continue to fuel shallow, silicic magmatism at Toba. This interpretation is consistent with (1) the type of magmas erupted at Pusubukit (mostly intermediate to mafic in composition but including some dacite), (2) the continuity of the column from the mantle to the upper crust, and (3) the seismic evidence of magma (or possibly magmatic gas) movement. A second column of low velocities, which is less intense than the one below Pusubukit but which also originates in the mantle, can be recognized below the southern end of Samosir Island. This column, which may also mark the path of ascending mafic melts, roughly corresponds with the zone of post-YTT dacite lava extrusion (Pardupur

Island), hydrothermal activity, and minor, recent doming.

7.2.1. Percent melt

[42] Although velocity structures beneath calderas and volcanic regions have been studied extensively, there is no unique method to relate in situ velocities to the proportion of melt. Murace and McBirney [1973] measured temperature-dependent velocities of compressional waves in several types of igneous rocks. The experiments showed that the compressional seismic wave speed is nearly constant at about 5–6 km/s below 800°–900°C and decreases by ~50% to 2–3 km/s in fully molten rocks at 1200°C. Velocity decreases do not reach 50% in the crust below Toba, indicating that no entire block in our three-dimensional *P* velocity model, each of which is 10 km on a side, is likely to be dominated by melt. This is consistent with the observation that Poisson’s ratio does not vary on a large scale in the one-dimensional velocity inversions. Considering, however, that our velocities are averages for each block (or for each layer in the one-dimensional case), the large decreases recorded (up to 37% below normal crustal V_p in this region) likely indicate melt-dominated domains on a smaller (<10-km-thick) scale.

[43] Our three-dimensional *P* velocity model also shows velocities in what is likely the uppermost mantle (40- to 65-km depth) beneath Toba of about 6.0–7.0 km/s, or about 14–26% below the normal *P* velocity of the upper mantle in this region and below typical continental areas. Mavko [1980] showed that *P* velocity reductions of 10–40% result from 10% partial melting of the upper mantle. Tests using different depths of the Moho indicate that the depth of these low velocities is at least 35 km beneath the depression. Because the low *P* velocities in the upper mantle are



beneath both the low velocities within the crust and the hypocenters of low-frequency earthquakes, we suggest that the low velocities reveal the mantle sources of the Toba magma system.

7.2.2. Comparison to other calderas

[44] Previous seismic studies have revealed low P velocities beneath the three young calderas in the western United States: the Valles caldera [Steck *et al.*, 1998; Lutter *et al.*, 1995; Roberts *et al.*, 1991; Ankeny *et al.*, 1986], the Long Valley caldera [Weiland *et al.*, 1995; Steck and Prothero, 1994; Dawson *et al.*, 1990], and the Yellowstone caldera [Miller and Smith, 1999]. The low-velocity regions are commonly interpreted as remnant magma chambers at shallow depth or mafic magmas ponded in the midcrust. At Valles caldera, P velocities are low by as much as 23% in an elliptical volume in the middle crust (5- to 16-km depth) below the northwest quadrant of the caldera, separated from a broad zone of low velocities (–15%) in the upper mantle [Steck *et al.*, 1998]. Beneath Long Valley caldera the maximum low velocities (–35 to –30%) are also in the middle crust, at ~11.5-km depth [Weiland *et al.*, 1995]. Similarly, a recent tomographic study at Yellowstone, using local earthquakes and controlled sources [Miller and Smith, 1999], revealed a broad low P velocity region (–15%) beneath the caldera at 6- to 12-km depth, coincident with a gravity low.

[45] In contrast to these other well-studied calderas, the largest region of anomalously low P velocities at Toba is shallower, with the largest volume in the upper 10 km of crust. Also, although low velocities characterize the mantle below the Valles caldera, there is no apparent continuity of low velocities from the mantle to the crust in either of the other magma systems, as there is at Toba.

8. Conclusions

[46] Tomographic study of seismic velocities in the crust and mantle below Toba reveals a main low-velocity region with its dominant volume in the upper 10 km of crust, perhaps encompassing an area as large as the southern two thirds of the present-day 100 × 30 km depression. In the middle crust, between 10- and 24-km depth, this volume narrows in size and appears to merge with a more focused, low-velocity region below Pusubukit volcano. This region of low velocities is even more focused in the lower crust (24–40 km) and can be traced into the uppermost mantle. A second, less well defined, deep crustal region of low velocity may underlie the southernmost end of the shallow low-velocity region as well.

[47] Consistent with previous interpretations [Knight *et al.*, 1986] that the depression is a complex structure that formed by coalescence of smaller calderas, the large region of low velocity is separated by a high-velocity zone from a second low-velocity region that underlies the northern end of Toba. Smaller in size than that which underlies the southern two thirds of the depression, the northern low-velocity region coincides with the location inferred for a caldera-forming eruption at 0.5 Ma. The main, southern low-velocity region, which coincides with a gravity low and with the site of resurgent doming, outlines the reservoir that fed a large ash flow eruption at 0.84 Ma and again at 0.074 Ma during emplacement of the 2800-km³ Youngest Toba Tuff.

[48] The low-velocity regions identified by tomography are interpreted as showing the distribution of partially molten rock in a large-volume crustal system with mantle roots. In this system, partially molten upper mantle feeds a semicontinuous flux of ascending melt that ponds and fans out somewhere in the 10- to 20-km-depth range. At these and possibly

greater depths we envision a complex region in which subduction-related melts are crystallizing, mixing with partial melts of crust, and differentiating to more silicic compositions that ultimately feed the shallow (<10-km-depth), large-volume, silicic magma chambers that fed ash flow eruptions as recently as 74 kyr ago. We interpret the tomographic results to indicate two separate chambers, contradicting speculation that the 100-km-long depression is underlain by a single, shallow magma body [Chesner and Rose, 1991]. We cannot, however, rule out the possibility that such a magma system existed in the past, or that the present system is not connected at depths where our spatial resolution is low.

Appendix A. Reliability Tests for the Three-Dimensional Model

[49] A commonly used method to assess the reliability of tomographic inversion results is evaluation of the diagonal of the resolution matrix. The resolution matrix provides an estimate of relative contributions of data and the a priori model to the final model. If the resolution matrix is equal to the identity matrix, then the model parameters are perfectly resolved or uniquely defined; otherwise, the model parameter is a linear combination of neighboring model parameters. In general, the smaller the damping factor, the better the resolution matrix, but also the larger the variance. We adjusted the damping to find the best trade-off between the variance and the resolution.

[50] The average diagonals of the resolution matrix of models 3D-2, 3D-2X5, and 3D-2Y5 are 0.74035, 0.63185, and 0.64784 respectively (Table 3). Because the diagonals of those three models are similar, here we discuss only the diagonal matrix map of model 3D-2. The diagonals of the resolution matrix for model 3D-2 around Toba are mostly >0.5, except along the

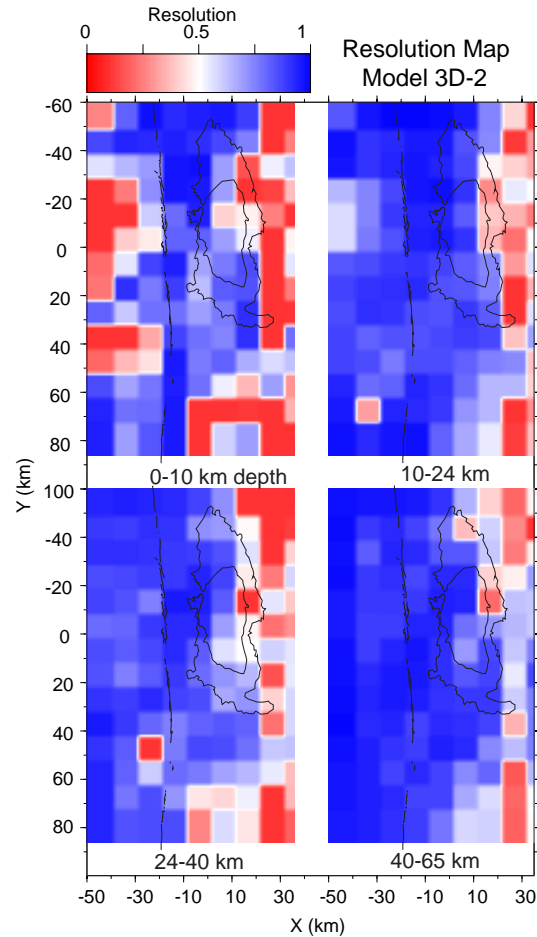


Figure A1. Resolution map of model 3D-2 superimposed on the outline of Toba Lake and the Sumatra fault.

eastern side of the depression (Figure A1). The low resolution northeast of Toba is caused by timing errors at broadband stations located on that side.

[51] In addition, checkerboard tests were conducted to assess the ability of the data and method to recover existing velocity anomalies within the model. The checkerboards were constructed by perturbing blocks within the model structure with a $\pm 10\%$ deviation from the average P within each layer. Three different checkerboard block sizes were tested: 5×5 km

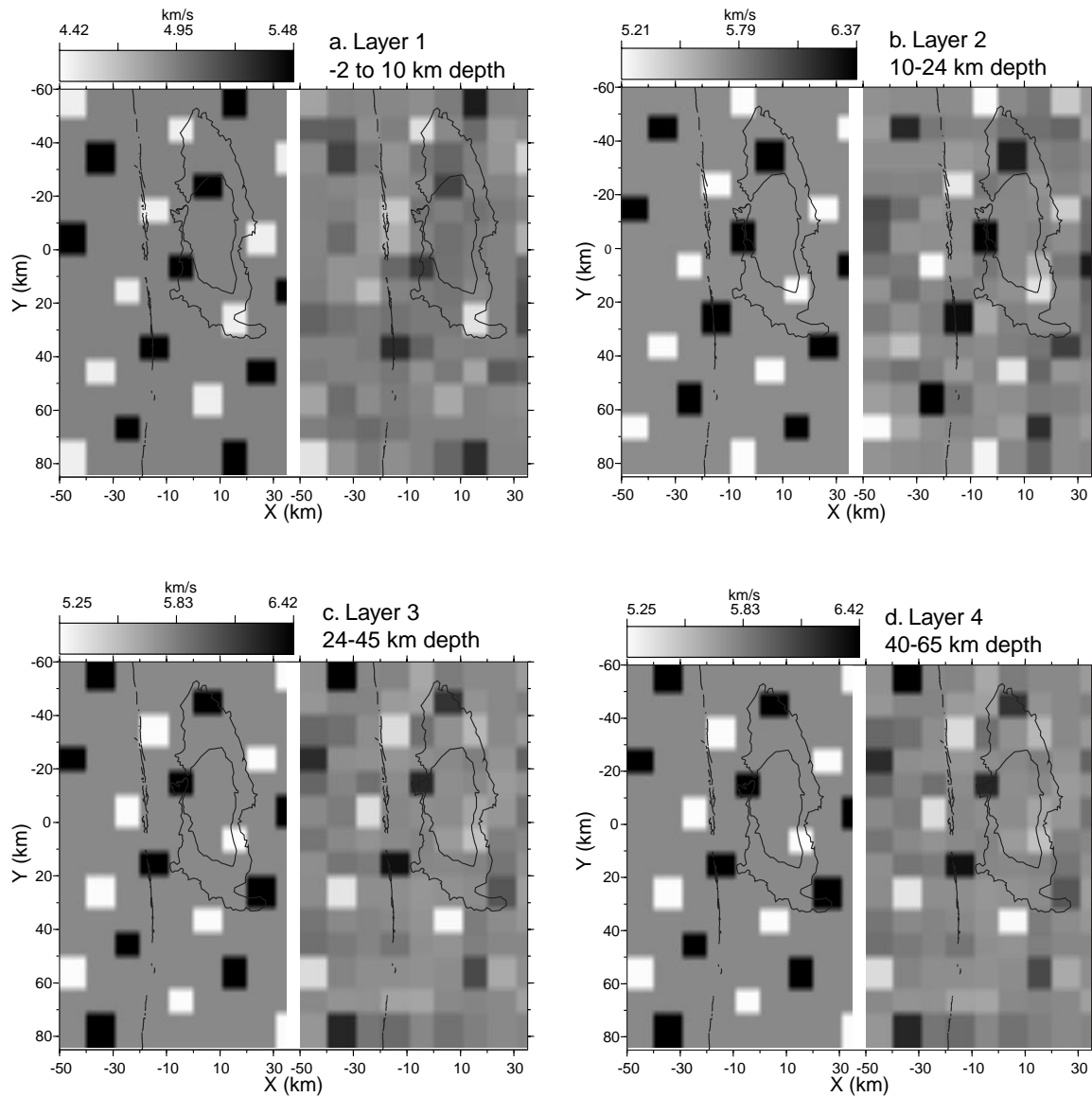


Figure A2. (a–d) Results of the checkerboard test for each layer. The lateral dimensions of the blocks are 10×10 km; the velocity anomaly is 10%. Random error with $\sigma = 0.1$ s is added to the synthetic data. In each panel the left is the test model, and the right is the recovered model.

(CB-1), 10×5 km (CB-2), and 10×10 km (CB-3). Synthetic P arrival time data were generated with the checkerboard structure, to which we added normally distributed random errors with standard deviation 0.1 s. We attempted to recover the structure using a block size of 10×10 km. Results of the inversions show that

CB-1 and CB-2 were not recovered, but CB-3 was recovered well (Figure A2). These tests suggest that a 10×10 km block with <50% volume of the 10% anomaly will not be recovered.

[52] Another test we applied is to use the final 3-D structure to calculate synthetic data with

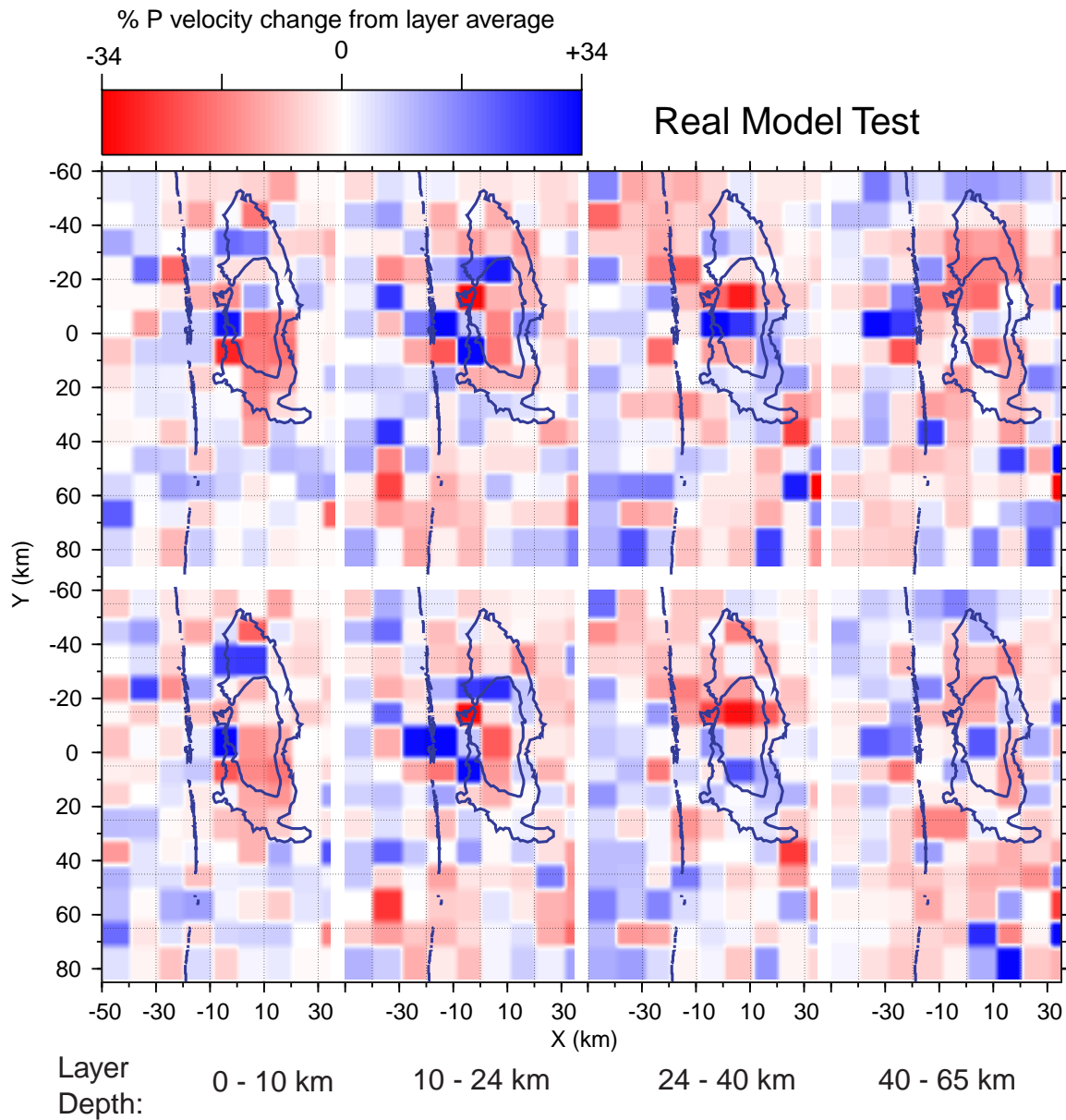
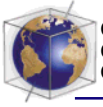


Figure A3. (a–d) Results of model resolution using the final model for each layer, presented in terms of fractional change from layer average. Synthetic data were calculated using the result of model 3D-1; random errors with $\sigma = 0.1$ s are added to the synthetic data. The model was recovered using a 10×10 block size. In each depth range the panel at the top is the 3D-1 model, and the panel at the bottom is the recovered model.

random noise added and then rerun the inversion to see if the same structure results. For this purpose, we computed synthetic data based on ray tracing through the final three-dimensional average model and using the same coverage as

the real data. Normally distributed random errors ($\sigma = 0.1$ s) were added to arrival times. The inversion was run for five iterations using a 10×10 km block size. In general, the main structures were recovered well, suggesting that

our result is reflecting real features beneath Toba (Figure A3).

Acknowledgments

[53] The PASSCAL field program was aided considerably by Paul Friberg, John Nabelek, Peter Zwick, Colleen Stevens, Yanuar, Sutrisno, Wandono, Safra Dwipa, Lukman, Safyan, Hendra, Edy Sukanto, and Kristianto. Doug Johnson, John Ebel, and Bill Menke made equipment available. Lee Steck and Craig Chesner made helpful comments, with Associate Editor Don Forsyth providing a particularly thorough review. Funded by NSF grant EAR-9316344.

References

- Abers, G. A., and S. W. Roecker, Deep structure of an arc-continent collision: Relation of earthquakes and inversion for upper mantle *P* and *S* wave velocities beneath Papua New Guinea, *J. Geophys. Res.*, **96**, 6379–6402, 1991.
- Aki, K., and R. Koyanogi, Deep volcanic tremor and magma ascent mechanism under Kilauea, Hawaii, *J. Geophys. Res.*, **86**, 7095–7109, 1981.
- Aki, K., and W. H. K. Lee, Determination of three-dimensional velocity anomalies under aseismic array using first *P* arrival times from local earthquake, 1, A homogeneous initial model, *J. Geophys. Res.*, **81**, 4381–4399, 1976.
- Aldiss, D. T., and S. A. Ghazali, The regional geology and evolution of the Toba volcano-tectonic depression, Indonesia, *J. Geol. Soc. London*, **141**, 487–500, 1984.
- Ankeny, L. A., L. W. Braile, and K. H. Olsen, Upper crustal structure beneath the Jemez Mountains volcanic field, New Mexico, determined by three-dimensional simultaneous inversion of seismic refraction and earthquake data, *J. Geophys. Res.*, **91**, 6188–6198, 1986.
- Armitage, J., S. Roecker, Masturyono, R. McCaffrey, J. Nabelek, and D. Wark, Receiver function analysis of broadband data in Toba caldera, Sumatra, *Eos Trans. AGU*, **80**(17), Fall Meet. Suppl., F666, 1999.
- Bevington, P. R., *Data Reduction and Error Analysis for the Physical Sciences*, 336 pp., McGraw-Hill, New York, 1969.
- Chesner, A. C., and W. I. Rose, Stratigraphy of the Toba Tuff and the evolution of the Toba Caldera Complex, Sumatra, Indonesia, *Bull. Volcanol.*, **53**, 343–356, 1991.
- Chesner, C. A., W. I. Rose, A. Deino, R. Drake, and J. A. Westgate, Eruptive history of Earth's largest Quaternary caldera (Toba, Indonesia) clarified, *Geology*, **19**, 200–203, 1991.
- Dawson, P. B., J. R. Evans, and H. M. Iyer, Teleseismic tomography of the compressional wave velocity structure beneath the Long Valley region, California, *J. Geophys. Res.*, **95**, 11,021–11,050, 1990.
- DeMets, C., R. G. Gordon, D. F. Argus, and S. Stein, Effects of recent revisions to the geomagnetic reversal time scale on estimates of current plate motions, *Geophys. Res. Lett.*, **21**, 2191–2194, 1994.
- Fauzi, Seismological studies of tectonics in the Toba region and the Banda Sea, Indonesia, Ph.D. thesis, Rensselaer Polytech. Inst., Troy, N. Y., 1999.
- Fauzi, R. McCaffrey, D. A. Wark, Sunaryo, and P. Y. Prih Haryadi, Lateral variation in slab orientation beneath Toba Caldera, northern Sumatra, *Geophys. Res. Lett.*, **23**, 443–446, 1996.
- Hasegawa, U., T. Okada, and A. Yamamoto, Deep low frequency microearthquakes in the northeastern Japan Arc, *Eos Trans. AGU*, **78**(46), Fall Meet. Suppl., F438, 1997.
- Jones, C. H., H. Kanamori, and S. W. Roecker, Missing root and mantle “drips”: Regional Pn and teleseismic arrival times in the southern Sierra Nevada and vicinity, California, *J. Geophys. Res.*, **99**, 4567–4601, 1994.
- Kennett, B. L. N. (Compiler and Editor), *IASPEI 1991 Seismological Tables*, 167 pp., Bibliotech, Canberra, Australia, 1991.
- Kiekhefer, R. M., Geophysical studies of the oblique subduction zone in Sumatra, Ph.D. thesis, 119 pp., Univ. of Calif., San Diego, 1980.
- Knight, M. D., G. L. Walker, B. B. Ellwood, and J. F. Diehl, Stratigraphy, paleomagnetism, and magnetic fabric of the Toba tuffs: Constraints on the sources and eruptive styles, *J. Geophys. Res.*, **91**, 355–382, 1986.
- Lutter, W. J., P. M. Roberts, C. H. Thurber, L. K. Steck, M. C. Fehler, D. G. Stafford, W. S. Baldrige, and T. A. Zeichert, Teleseismic P-wave image of crust and upper mantle structure beneath Valles caldera, New Mexico: Initial result from the 1993 JTEX passive array, *Geophys. Res. Lett.*, **22**, 505–508, 1995.
- Malone, S., Deep long-period earthquakes in the Washington Cascades, *Eos Trans. AGU*, **78**(46), Fall Meet. Suppl., F438, 1997.
- Masturyono, Imaging the magma system beneath Toba Caldera, north Sumatra and aftershock study of the 1996 Biak earthquake, Irian Jaya, Indonesia, Ph.D. thesis, Rensselaer Polytech. Inst., Troy, N. Y., 2000.
- Mavko, G. M., Velocity and attenuation in partially molten rocks, *J. Geophys. Res.*, **85**, 5173–5189, 1980.
- Miller, D. S., and R. B. Smith, *P* and *S* velocity structure of the Yellowstone volcanic field from local earthquake

- and controlled source tomography, *J. Geophys. Res.*, **104**, 15,105–15,121, 1999.
- Murace, T., and A. R. McBirney, Properties of some common igneous rocks and their melt at high temperatures, *Geol. Soc. Am. Bull.*, **84**, 3563–3593, 1973.
- Ninkovich, D., N. J. Shackleton, A. A. Abdel Munem, J. D. Obradovich, and G. Izzet, K-Ar age of Pleistocene eruption, of Toba, north Sumatra, *Nature*, **276**, 574–577, 1978.
- Nishimura, S., E. Abe, J. Nishida, T. Yokoyama, A. Dharma, P. Hehanusa, and F. Hehuwat, A gravity and volcanostratigraphic interpretation of Lake Toba region, north Sumatra, Indonesia, *Tectonophysics*, **109**, 253–272, 1984.
- Okubo, P., The significance of long-period seismicity in Hawaii, *Eos Trans. AGU*, **78**(46), Fall Meet. Suppl., F437, 1997.
- Pavlis, G. L., and J. R. Booker, The mixed discrete-continuous inverse problem: Application to the simultaneous determination of earthquake hypocenters and velocity structure, *J. Geophys. Res.*, **85**, 4801–4810, 1980.
- Pitt, A. M., and D. P. Hill, Occurrence of mid-crustal, long period earthquakes in northern California, *Eos Trans. AGU*, **78**(46), Fall Meet. Suppl., F438, 1997.
- Power, J. A., A. D. Jolly, M. L. Harbin, and C. J. Nye, Deep long-period events associated with the 1992 eruptions of Crater Peak Vent, Mont Spurr, Alaska, *Eos Trans. AGU*, **78**(46), Fall Meet. Suppl., F438, 1997.
- Roberts, P. M., K. Aki, and M. C. Fehler, A low-velocity zone in the basement beneath Valles caldera, New Mexico, *J. Geophys. Res.*, **96**, 21,583–21,596, 1991.
- Roecker, S. W., Y. H. Yeh, and Y. B. Tsai, Three-dimensional *P* and *S* wave velocity structures beneath Taiwan: Deep structure of an arc-continent collision, *J. Geophys. Res.*, **92**, 10,547–10,570, 1987.
- Roecker, S. W., T. M. Sabitova, L. P. Vinnik, Y. A. Burmakov, M. I. Golvanov, R. Mamatkanova, and L. Munirova, The three-dimensional elastic wave velocity structure of western and central Tien Shan, *J. Geophys. Res.*, **98**, 15,779–15,795, 1993.
- Shedlock, K. M., and S. W. Roecker, Elastic wave velocity structure of crust and upper mantle beneath the North China Basin, *J. Geophys. Res.*, **92**, 9327–9330, 1987.
- Sieh, K., and D. Natawidjaja, Neotectonics of the Sumatran fault, Indonesia, *J. Geophys. Res.*, **105**, 28,295, 2000.
- Smith, R. L., and R. A. Bailey, Resurgent cauldron, in *Study in Volcanology*, edited by R. R. Coat, R. L. Hay, and C. A. Anderson, *Mem. Geol. Soc. Am.*, **116**, 613–668, 1968.
- Steck, L. K., and W. A. Prothero Jr., Crustal structure beneath Long Valley caldera from modeling of teleseismic *P* wave polarization and *P* converted wave, *J. Geophys. Res.*, **99**, 6881–6898, 1994.
- Steck, L. K., C. H. Thurber, M. C. Fehler, W. J. Lutter, P. M. Robbert, W. S. Baldrige, D. G. Stafford, and R. Sessions, Crust and upper mantle *P* wave velocity structure beneath Valles caldera, New Mexico: Result from the Jemez teleseismic tomography experiment, *J. Geophys. Res.*, **103**, 24,301–24,320, 1998.
- Tarantola, A., and B. Valette, Generalized nonlinear inverse problems solved using the least-squares criterion, *Rev. Geophys.*, **20**(2), 219–232, 1982.
- Thurber, C. H., and W. L. Ellsworth, Rapid solution of raytracing problem in heterogeneous media, *Bull. Seismol. Soc. Am.*, **70**, 1137–1148, 1988.
- Ukawa, M., Deep low frequency earthquakes beneath volcanic front in central Japan, *Eos Trans. AGU*, **78**(46), Fall Meet. Suppl., F438, 1997.
- Van Bemmelen, R. B., The volcano-tectonic origin of Lake Toba (north Sumatra), *De Ing. Ned Indie*, **6–9**, 126–140, 1939.
- Verstappen, H. T., Some volcano-tectonic depressions of Sumatra, their origin and mode of development, *Proc. K. Ned. Akad. Wet., Ser. B Phys. Sci.*, **64**, 428–443, 1961.
- Wark, D. A., Masturyono, R. McCaffrey, G. L. Farmer, M. Rani, and R. Sukhyar, Plumbing of the Toba magma system: Petrologic and geophysical evidence of two shallow reservoirs and their mantle roots, *Eos Trans. AGU*, **81**, Fall Meet. Suppl., F1387, 2000.
- Warren, L., D. Gillard, and A. Rubbin, Similar long-period earthquakes beneath Kilauea Volcano, *Eos Trans. AGU*, **78**(46), Fall Meet. Suppl., F437, 1997.
- Weiland, C., L. K. Steck, P. Dawson, and V. Korneev, Crustal structure beneath Long Valley caldera from non-linear teleseismic travel time tomography using three-dimensional ray, *J. Geophys. Res.*, **100**, 20,379–20,390, 1995.
- White, R. A., and D. Dzurisin, Deep long period earthquake: Seismic evidence of rising basalt, *Eos Trans. AGU*, **78**(46), Fall Meet. Suppl., F437, 1997.
- Yokoyama, T., and P. E. Hehanusa, The age of “old Toba tuff” and some problem on geohistory of Lake Toba, Sumatra, Indonesia, Paleolimnology of Lake Biwa, Jpn, *Pleistocene*, **9**, 177–186, 1981.